Combining Photocatalysis and Optical Fibre Technology towards improved Microreactor Design for Hydrogen Generation with Metallic Nanoparticles

Matthew E. Potter[a]*, Daniel J. Stewart[a], Alice E. Oakley[a], Richard P. Boardman[b], Tom Bradley[c], Pier J. A. Sazio[c] and Robert Raja[a]

a) Department of Chemistry, University of Southampton, Highfield Campus, Southampton, Hampshire, SO17 1BJ, UK.

b) Mu-Vis X-ray Imaging Centre, University of Southampton, Highfield Campus, Southampton, Hampshire, SO17 1BJ, UK.

c) Optoelectronics Research Centre, University of Southampton, Highfield Campus, Southampton, Hampshire, SO17 1BJ, UK.

* M.E.Potter@soton.ac.uk

Abstract

The use of solar energy to activate chemical pathways in a sustainable manner drives the development in photocatalysis. While catalyst optimisation is a major theme in this pursuit, the development of novel photocatalytic reactors to enhance productivity is also imperative. In this work we combine, for the first time, microstructured optical fibre technology with photocatalysis, creating a photocatalytic microreactor coated with TiO_2, decorated with palladium nanoparticles. In doing so, we create a system capable of effectively combining photons, liquids and gases within a monolithic, highly confined, transparent silica geometry. We utilise a range of characterisation techniques to selectively focus on the photocatalyst, that resides exclusively within the internal capillaries of this system. In doing so we validate our design approach, and demonstrate the ability to simultaneously control both nanoparticle size and metal content. Further, we justify our unique design, showing its activity in photocatalytic hydrogen generation from water. In doing so highlighting the importance in developing light propagation properties from optical fibres, and the significant potential of this technology in the expansive photocatalysis landscape.

Keywords

Photonics, Catalysis, Optical-fibre, Solar Energy, Hydrogen Production, Nanoparticles, Tomography

Introduction

Establishing the 21st century as the first environmentally conscious era in human history, brings significant challenges for science and technology.[1,2] As a society we are aware of our devastating environmental impact. Therefore the demand for economically feasible solutions to renewable energy, elimination of greenhouse gases and sustainable chemical production is now extremely urgent.[3] Catalysis will always be at the forefront of sustainable innovation, as improved rates of chemical production, under less intensive conditions, bring both economic and environmental benefits.[4] Most processes require heat to initiate the catalytic cycle, though many are now taking inspiration from the natural world, utilising solar power for the generation of chemical energy.[5,6] This has seen interest grow in hydrogen generation from photocatalytic water splitting.[7-10] A common vision for the future sees CO_2 reduction as a significant contributor to chemical and fuel production.[11,12] Thus, a sustainable source of hydrogen is needed before widespread CO_2 reduction can be sustainable.

Photochemical hydrogen generation from water has been studied by many groups, leading to a plethora of catalytic systems,[7-10,13,14] for both direct (water forms hydrogen and oxygen without additives) and indirect (using a sacrificial reagent) water splitting. Despite many developments in this field, titania (TiO_2) is still heavily utilised, due to its availability, low cost and high activity.[7-10] The band gap of TiO_2 (3.6 eV) means it is well suited to applications with UV light, though is less effective with visible light. TiO_2 can be modified to increase activity, commonly by introducing dopant atoms, either bringing reagents closer to the active site, or altering the rate-determining step, increasing reactivity.[15] In photocatalysis, dopants also create multiple p-n junctions,[16] increasing photon efficiency, or increasing the range of active light.[17] When screening a range of dopants on TiO_2, Bowker *et al* showed that Pd nanoparticles significantly improved hydrogen yields for photocatalytic water splitting, as they expanded the range of light that could be used.[18] Further, it was demonstrated that suspending the catalyst above the alcoholic water solution, not in contact with the liquid, enhanced the activity,[19] emphasising the need for careful reactor design in photochemical processes.

The boom in optical fibre technology has played a major role in telecommunications, data storage and networking.[20,21] Variations in cladding and the range of fibre motifs, can prompt many distinct optical phenomena.[22,23] Ultimately these variables led to these waveguides having unprecedented control of light propagation, amplification and emission. Optical fibre technology has started to play an active role in photocatalysis, as their control of light makes them uniquely suited as photon delivery systems. An example of this from Denny *et al*, shows how two distinct optical fibre types were contrasted to create an effective light source within a photoreactor, for the degradation of oxalic acid using glass beads coated with TiO_2.[24] Another strategy from Maroto-Valer *et al* utilises a monolith coated with photocatalytic species, which is subsequently threaded with optical fibres, allowing light to refract onto the coated monolith channels. In doing so it was possible to introduce dopants onto the monolith, enhancing CO_2 reduction, achieving orders of magnitude improvements in quantum efficiency over a conventional slurry batch annular reactor.[25]

More recently, microstructured optical fibre canes (MOFCs) have been developed as high pressure microfluidic reactors, where each cane houses multiple capillaries running the length of the cane.[26] Modifications are possible during the fabrication (drawing) procedure, including utilising doped silica species, to vary the composition of the cane,[27] though these are limited due to the extreme conditions used in a pull; however post-synthesis options are available. Chemical Vapour Deposition (CVD) has been shown to coat the interior of these canes, giving them catalytic potential, but this requires high pressures and unstable reagents such as metal hydrides.[28] In this work we discuss our unique design methodology for transforming MOFCs into photocatalytic microreactors. This multi-step procedure utilises the improved internal surface area, and capillary shape of the MOFCs to selectively coat the internal capillaries with TiO_2, doped with palladium nanoparticles. This new technology allows the coated canes then simultaneously serve as both host and catalyst for the continuous indirect water splitting to yield hydrogen, with methanol as a sacrificial reagent. Photons, gases and fluids are thus confined within a highly scalable, thermomechanically robust, optically transparent silica monolith microreactor. This work establishes our novel design procedure, serving as proof-of-concept, to establish a range of wider studies on this theme, leading to unique catalytic applications and development of new characterisation protocols to understand such species.

Experimental

Cane deposition

MOFCs 10 cm in length were first coated using a suspension of 1 wt% commercial P25 TiO_2 nanopowder (Sigma-Aldrich) in water. The canes were then filled with the suspension using at a rate of 5 cm/min using a syringe pump. The suspension was then removed by forcing air through the system, again using a syringe pump, at a speed of 3 cm/min. This procedure was then repeated from the other end of the cane to achieve an even coating. The sample was subsequently dried overnight at 70 ^oC, and then heated in an air atmosphere at 400 ^oC for 4 hrs, at a ramp rate of 5 ^oC/min. These systems are labelled as TiO_2/MOFC.

Pd nanoparticles were then deposited onto the fibre using a colloidal surfactant procedure.(29) 0.38 mL of an aqueous 10.6 mg/mL K_2PdCl_4 solution and 0.20 mL of an aqueous 6.50 mg/mL polyvinylpyrollidone (PVP) solution were added together in 80 mL of methanol. The system was stirred for 10 minutes when 0.51 mL of an aqueous 0.1 M $NaBH_4$ solution was added dropwise. This gave a final Pd concentration of 0.05 mg/mL. Two other 80 mL solutions were also used where the quantities of the K_2PdCl_4, $NaBH_4$ and PVP were increased by a factor of 3 or 9, to give final Pd concentrations of 0.15 and 0.45 mg/mL. The system was left to stir for 2 hours, before the TiO_2/MOFC canes were added and left to stir for 1, 3 or 18 hours. The final systems were labelled as: X-Pd-Y/TiO_2/MOFC where X represents the concentration of the Pd nanoparticle solution (either 0.05, 0.15 or 0.45 mg/mL) and Y represents the deposition time (either 1, 3 or 18 hrs). The systems were then dried at 70 ^oC overnight and were then ready for use.

Computerised Tomography

Computerised tomography (CT) images were collected at the µ-Vis imaging centre at the University of Southampton. Images were acquired on the Zeiss 160 kVp Versa 510 system. X-ray tomographic imaging was performed using a Zeiss Xradia Versa 510 system. Scans were performed at three different resolutions, with an energy of 50 kVp and current of 80 µA. 1601 projections were captured for each scan. No filtration was used on the beam, and the source to object distance was 10.02 mm, and the object to detector distance was 6.04 mm. The scan performed at 4x magnification yielded a resolution of 2.084 µm per voxel, with an exposure time of 2 seconds. Subsequent scans were performed at 20x and 40x magnification, with respective exposure times of 15 and 25 seconds per projection. The voxel resolution of the 20x scan was 830 nm, and the 40x scan 420 nm.

Microfocus X-ray Absorption Spectroscopy

Microfocus X-ray absorption spectroscopy was performed at I18 at the Diamond Light Source, Didcot, UK *via* standard access proposal SP17819. Fluorescence maps were used to identify titania rich areas, scanning an area 400 µm x 400 µm. XANES (X-ray Absorption near Edge Spectroscopy) of TiO_2 rich areas were then collected from 4.9 to 5.2 keV. X-ray diffraction patterns were collected at 17 keV.

Results and Discussion

Cane production

A Kagome lattice cane[30] was chosen as the tessellated hexagonal and triangular channels will provide different sites for catalyst deposition, allowing us to contrast their behaviour, aiding future designs. The integrity of the 1/8" in diameter silica canes was confirmed using microscopy images post-production (Figure 1). This showed the intended Kagome lattice structure, tessellated with triangles and hexagons, the latter with a diameter of around 240 µm. The produced canes were a metre in length, though cut down to 10-15 cm for the purposes of this work.

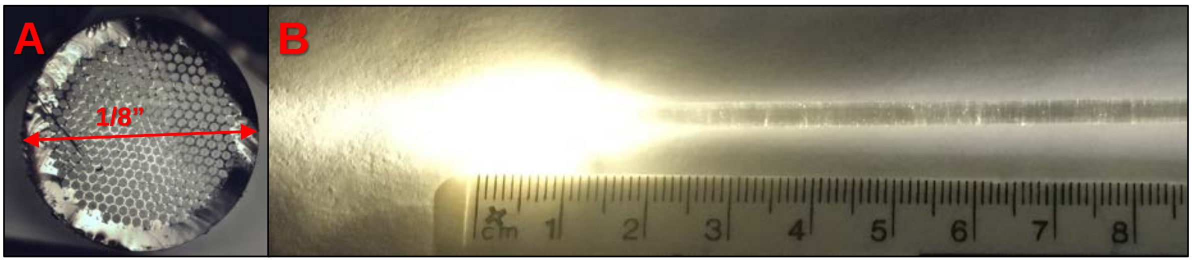

Figure 1: Images showing A) the presence of multiple hexagonal and triagonal capillaries in a Kagome lattice and B) the light propagation of these canes.

TiO_2 coating

Inductively coupled plasma (ICP) data of the P25 TiO_2 coated cane shows titanium makes only a tiny contribution of the total system (< 0.1 wt%), as such conventional characterisation methods can only provide limited information. Initial microscopy images show a build-up of powder in the triangular capillaries, which will allow photons, gases and fluids to simultaneously interact within these channels. This was confirmed using computerised tomography. 2D image stacks show that TiO_2 was primarily deposited in the triangular faces, with minimal deposition in the hexagonal channels. A video showing the variation in the xy plane moving down the length of the cane (z-axis) also confirms this with spots of TiO_2 appearing, again mainly in the triangular corners. The 3D reconstruction (Figure 2) highlights the surface roughness and deposits of bright TiO_2 spots in the triangular sections also, with the hexagonal channels comparatively empty. The reconstruction shows the lack of uniformity in the coating process, with scope for improvements to achieve a more consistent coating.

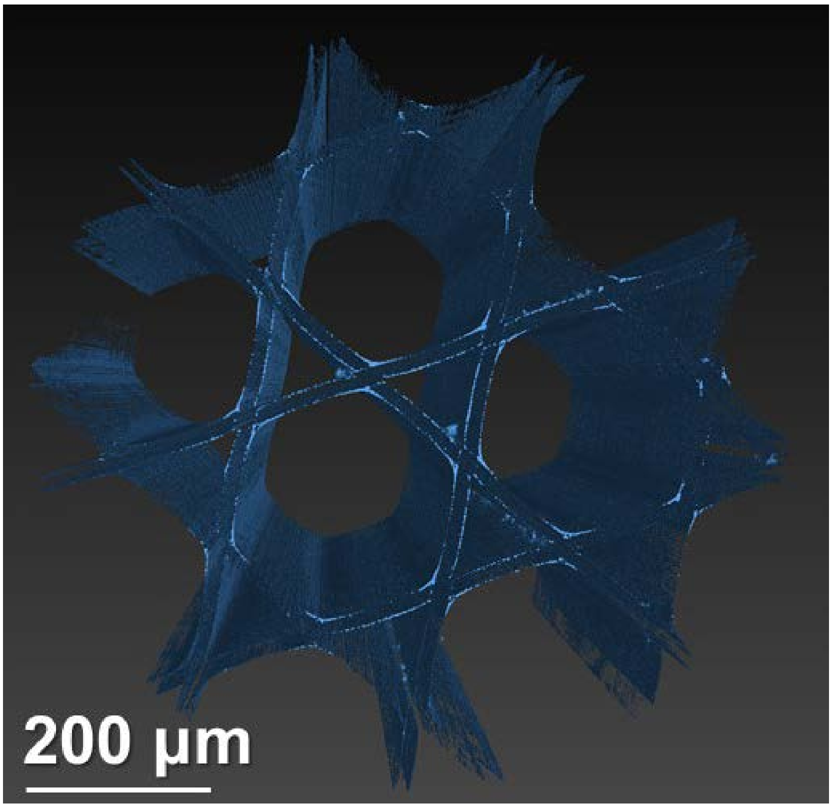

Figure 2: Computerised tomography of a section of TiO_2/MOFC with resolution of 830 nm, collected at an energy of 50 kVp and a current of 80 µA, showing build-up of TiO_2 (light blue particles) in the triangular channels.

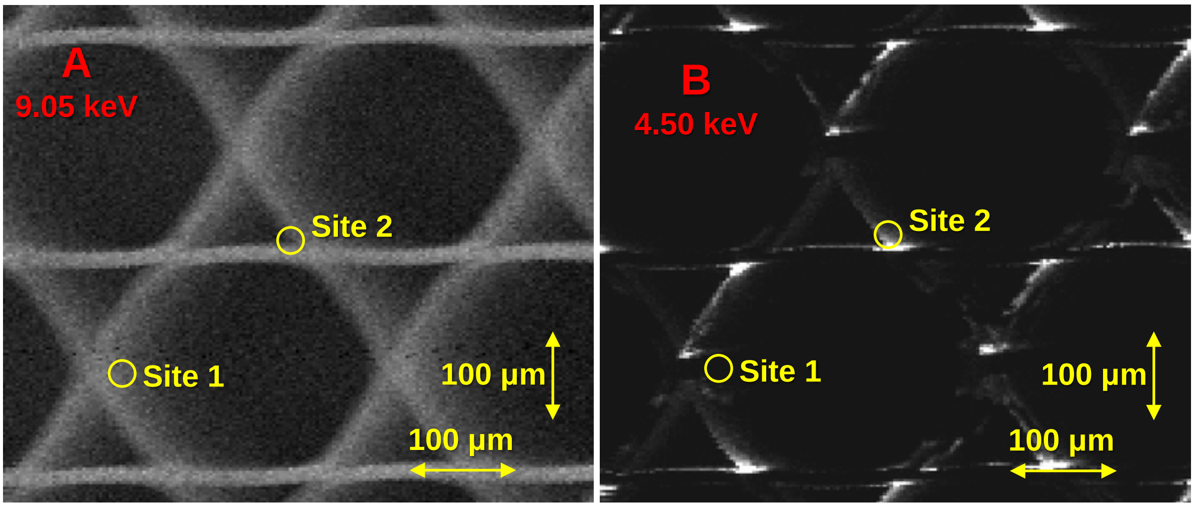

Figure 3: X-ray fluorescence maps collected at I18 Diamond light source, at an incidence energy of A) 9.05 keV showing the Kagome lattice structure of the fused silica canes, and B) 4.50 keV to highlight the Ti rich areas where P25 TiO_2 has been deposited.

The deposited TiO_2 was analysed using microfocus X-ray absorption spectroscopy for both X-ray diffraction and XANES measurements on the TiO_2 region. Initially a fluorescence map, collected at 9.05 keV incidence energy (Figure 3A), clearly shows the Kagome lattice. From this, two sites were chosen to contrast the bare cane (hexagonal wall, site 1) and a TiO_2 rich area (triangular wall, site 2). The energy-scanned fluorescence spectra of site 1 (shown in Figure S4), on the wall of a hexagonal channel, shows very little features apart from the refracted incidence energy at 9.05 keV. This agrees with the original microscopy and CT images (Figures 1 & 2), suggesting there is little deposition in the hexagonal channels. A smaller feature is seen at around 3 keV, which is attributed to argon from the air. Collecting analogous measurements on site 2 also shows the signal at 9.05 keV, however features at 4.50 and 4.93 keV are also noticeable (Figure S4), which are attributed to the Ti $K_{\alpha1}/K_{\alpha2}$ and Ti K_{β} transitions respectively. This therefore confirms significant amounts of Ti (TiO_2) are present in this region. Collecting a fluorescence map for the same region at 4.50 keV (Figure 3B) highlights the areas rich in titania, again showing it is preferentially deposited in the triangular corners, with minimal deposition in the hexagonal channels. This is likely due to the smaller angles in these channels helping to trap and deposit TiO_2.

X-ray diffraction measurements of site 2 (Figure 4A) show a mixture of anatase (A) and rutile (R) phases, in good agreement with published data on P25 TiO_2.[(31)] There is significant noise below 20 °, attributed to the interference and influence of the silica canes. The proportion of the different phases confirms that both structural phases in P25 are maintained.

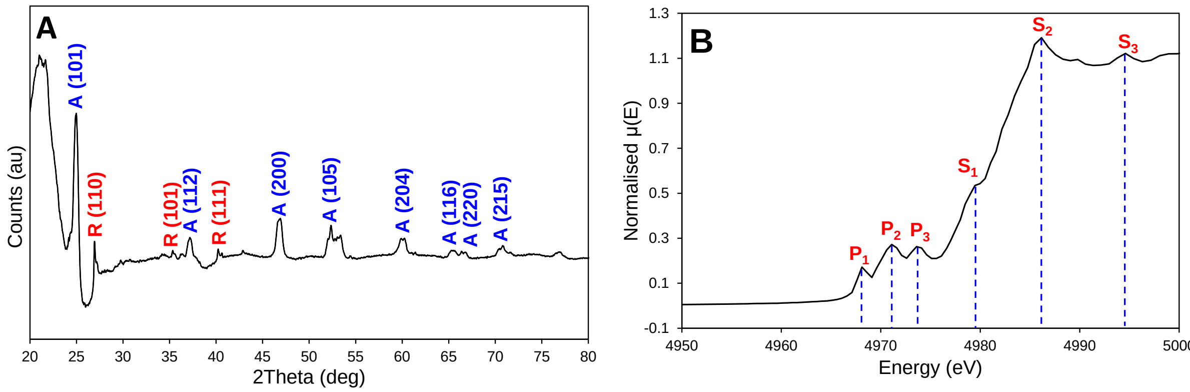

Figure 4: Taken from site 2 in Figure 3, showing A) X-ray diffraction pattern collected at 17 keV, from site 2 (Ti rich) showing both anatase and rutile phases, and B) XANES data showing a typical P25 TiO_2 spectra.

Ti XANES spectra of site 2 (Figure 4B) is also in excellent agreement with published data, showing pre-edge features (P_1, P_2 and P_3) at 4968, 4971 and 4974 eV respectively.[(32)] These features correspond to dipole-forbidden transitions from 1s to the 3d-4p hybrid orbital, t_{2g} and e_g respectively, confirming the octahedral and oxidic nature of the titanium. This region is typically convoluted by the rutile and anatase phases present, with the anatase features being more prominent, despite only comprising 15 % of the titania. In the main edge region we observe three spectral features; S_1, S_2 and S_3 (4979, 4986 and 4995 eV). S_1 corresponds to the shakedown process, whereas S_2 and S_3 represent the transitions from the 1s to the out-of-plane $4p_z$ and in-plane $4p_{x,y}$ orbitals.[(31)] S_1 and S_2 are typical of the anatase phase, whereas S_3 is indicative of the rutile phase, again confirming a combination of phases are still present.[(31)] Despite the low loading of TiO_2 in the system we have determined the preferred deposition location, and confirmed the biphasic nature of the P25 has been preserved.

Pd nanoparticle deposition

Polyvinlypyrrolidone (PVP) was used as a surfactant to generate a narrow distribution of Pd nanoparticles,[(29)] for subsequent deposition onto the P25 TiO_2, within the coated MOFC. The concentration of the Pd solution was varied from 0.05 to 0.15 and 0.45 mg/mL, with deposition time was varying from 1, 3 and 18 hours, to optimise the loading and nanoparticle size in the systems. The samples were labelled as X-Pd-Y/TiO_2/MOFC where X represents the concentration of the Pd nanoparticle solution (either 0.05, 0.15 or 0.45 mg/mL) and Y represents the deposition time either 1, 3 or 18 hrs).

ICP analysis (Table S1) shows despite changing the Pd concentration of the solutions, only a subtle increase in Pd content for MOFC samples occurs at a constant deposition time of 3 hours. Pd contents of 53, 58 and 77 ppm were found from solutions with concentrations of 0.05, 0.15 and 0.45 mg/mL respectively. However deposition time has a greater influence on Pd content, as varying the deposition time from 1, 3 and 18 hrs for a 0.15 mg/mL Pd solution, results in 48, 58 and 120 ppm of Pd content. These findings suggest that the Pd loading of the Pd-doped MOFC systems could be tuned through deposition time, to achieve specific metal loadings. These low Pd loadings and 'bulky' fused silica matrix mean many typical characterisation methods are not feasible for these systems. Preliminary UV/Vis data (Figure S5) showed a large feature at 300-400 nm, characteristic of octahedral titanium, as expected for rutile and anatase TiO_2.[33] However, no features attributed to Pd were seen, therefore, we explored the Pd active site using XANES and EXAFS techniques. We compared the MOFC systems with pelletized catalysts, with the same metal precursor concentrations and deposited for 18 hours.

The XANES of the pelletized Pd/TiO_2 species align well with the Pd Foil, confirming their metallic nature (Figures 5A & S6).[34] Some variations in intensity exist in the features at 24370 and 24390 eV, with the pelletized nanoparticle materials showing less defined features. This is likely due to the lack of bulk structure, and increased contribution from the PVP surfactant at the nanoparticles surface. As the concentration of the precursor solution increase, the intensity of the 24390 eV peak increases relative to the 24370 eV peak. This suggests the more concentrated precursor solution forms larger nanoparticles, with more bulk structure, more closely resembling the Pd foil. This trend is also seen in the $|\chi(R)|$ spectra (Figures S7 & S8), as increased precursor concentration increases the peak at 2.5 Å, this is also seen as the second shell Pd-Pd signals (4.5 and 5.1 Å) are more intense as the precursor concentration increases.

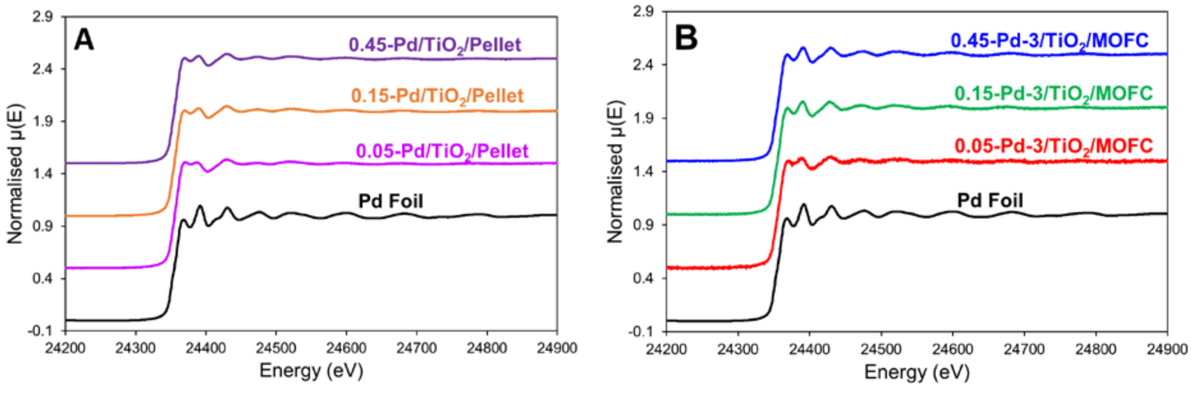

Figure 5: XAS spectra comparing A) pelletised powder samples of Pd/TiO_2 with B) analogous Pd/TiO_2/MOFC systems prepared with equivalent Pd precursor concentrations. Spectra stacked by 0.4 in μ(E) for clarity.

Table 1: EXAFS fitting parameters for Pd/TiO_2 systems in both pellet form and within a MOFC.

Sample	**Abs Sc**	**N**	**R / Å**	**$2\sigma^2$ / Å^2**	**E_f / eV**	**R_{factor}**
Pd Foil	Pd-Pd	12[a]	2.74 (1)	0.005 (2)	-6.6 (5)	0.01

0.05-Pd/TiO_2/Pellet	Pd-C	3.9 (5)	2.03 (1)	0.007 (3)	-1.7 (12)	0.03
	Pd-Pd	5.6 (5)	2.76 (1)	0.010 (2)		
0.15-Pd/TiO_2/Pellet	Pd-C	2.3 (3)	2.02 (1)	0.006 (1)	-2.4 (6)	0.01
	Pd-Pd	6.4 (3)	2.74 (1)	0.008 (1)		
0.45-Pd/TiO_2/Pellet	Pd-C	1.0 (1)	2.01 (3)	0.006 (3)	-4.7 (4)	0.01
	Pd-Pd	7.9 (4)	2.74 (1)	0.008 (1)		
0.05-Pd-3/TiO_2/MOFC	Pd-C	2.7 (2)	2.03 (1)	0.007 (4)	-7.9 (3)	0.01
	Pd-Pd	6.2 (1)	2.75 (1)	0.008 (3)		
0.15-Pd-1/TiO_2/MOFC	Pd-C	1.8 (4)	2.01 (1)	0.007 (4)	-7.3 (5)	0.01
	Pd-Pd	7.8 (3)	2.75 (2)	0.008 (2)		
0.15-Pd-3/TiO_2/MOFC	Pd-C	1.4 (2)	2.01 (1)	0.001 (2)	-7.5 (4)	0.01
	Pd-Pd	8.0 (1)	2.76 (2)	0.008 (1)		
0.15-Pd-18/TiO_2/MOFC	Pd-C	1.3 (2)	2.01 (2)	0.005 (2)	-7.0 (5)	0.01
	Pd-Pd	8.0 (1)	2.75 (1)	0.008 (1)		
0.45-Pd-3/TiO_2/MOFC	Pd-C	0.9 (3)	2.01 (2)	0.002 (3)	-7.1 (4)	0.01
	Pd-Pd	8.7 (3)	2.74 (1)	0.001 (1)		

Fitting parameters: S_0^2 = 0.812 (as per Pd foil), 3 < k < 12, 1 < R < 3, 11.2 independent points. a) Coordination number of the reference foil was held at 12 to determine the S_0^2 value.

Fitting the EXAFS data (Table 1) of the pelletised materials shows a strong Pd-Pd influence in all three materials, though a Pd-C path was also required to achieve a reasonable fit. This is attributed to Pd-PVP interactions on the surface of the nanoparticle, fits were attempted using Pd-N or Pd-O paths, instead of Pd-C, though these were unsuccessful. As the precursor concentration increases there is a greater proportion of the Pd-Pd path and less from Pd-C. This also agrees that increased precursor concentration leads to larger nanoparticles, with a greater proportion of 'bulk' Pd and a lower contribution from the surface.

Comparing the EXAFS data of the MOFC samples with the Pd foil (Figures 5B, S9, S10 & S11) also shows strong agreement in the XANES region, confirming that palladium in the MOFC samples is primarily in the metallic state. Unlike the Pd content (Table S1), the deposition time appears to have little influence on the XAS spectra. The three MOFC samples prepared with a 0.15 mg/mL solution, are near identical in the XANES and EXAFS region (Figure S12), despite significant differences in metal loading. The palladium precursor concentration was found to have minimal effect on the Pd content, though it has a notable influence on the EXAFS fitting parameters, primarily the Pd-Pd coordination number, similar to the pellets (Figure S13). Increasing the Pd concentration makes the EXAFS and XANES region more closely resemble the Pd foil, increasing the Pd-Pd interactions, and reducing the Pd-C interactions (Table 1). This is attributed to the formation of larger particles with greater 'bulk' contribution. The data quality noticeably increases from 0.05-Pd-3/TiO_2/MOFC to 0.45-Pd-3/TiO_2/MOFC, due to the increased Pd content (Table S1).

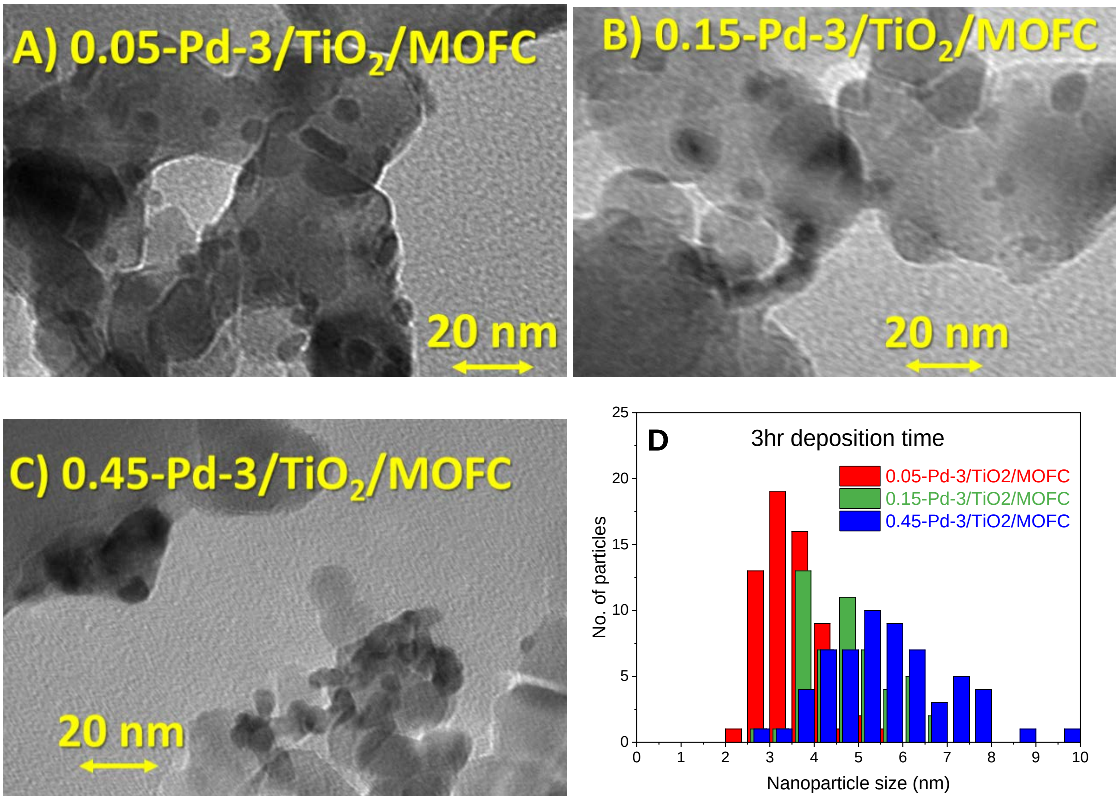

Figure 6: TEM images collected at an accelerating voltage of 100 kV, showing the influence of Pd solution concentration on Pd nanoparticle size, when deposited for 3 hrs from a crushed powder of A) 0.05-Pd-3/TiO_2/MOFC, B) 0.15-Pd-3/TiO_2/MOFC, C) 0.45-Pd-3/TiO_2/MOFC and D) the Pd nanoparticle size distributions.

The EXAFS and ICP data were complemented with transmission electron microscopy (TEM) images (Figures 6 & S14) to probe the size of the Pd nanoparticles in the systems, using a powder of the crushed cane. As such the samples are a mixture of fused silica, 21 nm P25 TiO_2 and Pd nanoparticles, as seen in various images (Figure 6 and S14). High resolution images of the systems were used to probe the influence of the Pd concentration and deposition time (Figures 6 and S14) on Pd nanoparticle size. Particles of P25 TiO_2 are readily observed at sizes of around 21 nm, which are decorated with Pd nanoparticles. A range of nanoparticle sizes are visible in the range of 2 – 8 nm across the different systems (Figures 6, S14 and S15). Plotting the nanoparticle size distributions (Figure S15) shows that the average nanoparticle size doesn't vary noticeably with deposition time (Figures 6B, S15B and S15C) between 1, 3 and 18 hrs (4.9, 4.7 and 4.7 nm respectively) for the 0.15 mg/mL series. The nanoparticles created from the 0.05 mg/mL Pd solution gave a smaller average nanoparticle size of 3.6 nm, in good agreement with the literature, which suggested this method would form nanoparticles between 2 – 4 nm.[29] At the highest Pd solution concentration (0.45 mg/mL) we observe a higher proportion of larger Pd nanoparticles (Figures 6 and S15F), with an average size of 5.6 nm. Not only does the higher Pd concentration promote the formation of larger particles, we also observe clustering of the nanoparticles (Figure 6C) in many places, thus they are less isolated, which could influence catalytic activity. The polydispersity index (PdI)[35] was calculated for the six systems (Table S2), in all cases the values were below 0.1, suggesting the nanoaprticles are monodisperse.[35] We note that the PdI shows little variation when concentration is constant, but deposition time varies (0.034, 0.045 and 0.045 for

1, 3 and 18 hrs deposition time respectively, at a Pd precursor concentration of 0.15 mg/mL. In contrast the PdI significantly increases when the deposition time is constant, but the Pd precursor concentration changes (0.038, 0.045 and 0.063 for 0.05, 0.15 and 0.45 mg/mL respectively for a deposition time of 3 hrs). This again shows that a greater distribution of nanoparticle size is observed at higher Pd concentrations. Calculation of the shape factor (comparing the highest and lowest dimensions of each particle, supplementary information, page S5), consistently gives values between 1.2 and 1.4. This shows the particles are not spherical (circular in our 2D TEM images), however instead form ellipsoids. Further information could be achieved through a more in-depth microscopy study, however this is beyond the scope of this work. The TEM findings discussed are in good agreement with our findings from the Pd-Pd EXAFS distances (Table 1), which also suggest that deposition time had limited influence on the palladium nanoparticles size, but Pd concentration of the solution could effectively modify the size.

Photocatalytic indirect water splitting

Methanol was chosen as a sacrificial reagent to aid water splitting for hydrogen generation, for ease of comparison with the current literature.[36-38] Though CO_2 is produced in this process ($CH_3OH + H_2O \rightarrow 3H_2 + CO_2$), the 3:1 stoichiometric ratio of H_2:CO_2 improves on conventional hydrogen production methods. Our design strategy combines the inherent activity of Pd/TiO_2, with the excellent light propagation properties of optical fibre technology. Therefore MOFC canes were tested with varying metal precursor concentrations and deposition times, whilst the volume of hydrogen was measured over an 8 hour period. Control reactions, using a non-coated MOFC, produced < 0.001 mL of hydrogen after 8 hours, confirming it was inactive. Similarly a TiO_2 coated MOFC cane (without Pd deposition) was also tested and also produced < 0.005 mL of hydrogen after 8 hours. This confirms that the Pd nanoparticles are required to induce meaningful photocatalytic activity.

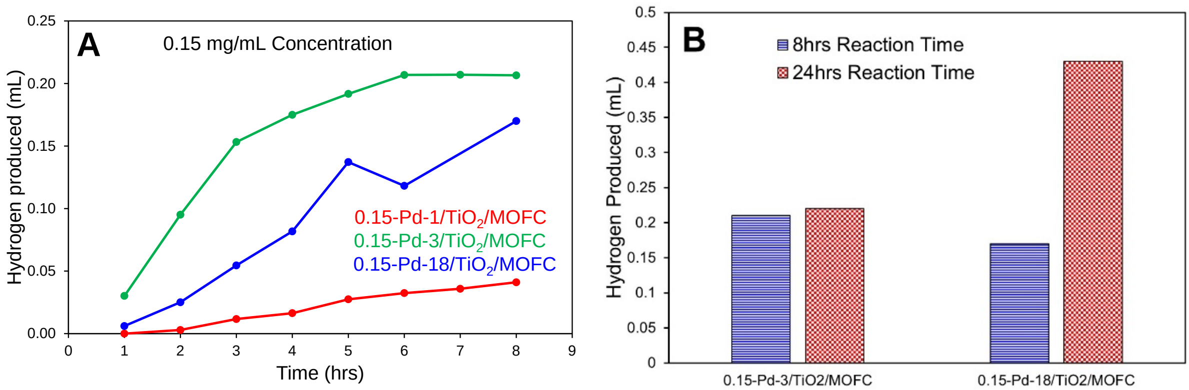

Figure 7: Photocatalytic data for the generation of hydrogen form methanolic water of the MOFC systems, collected at room temperature (25 °C) and pressure (1 atm), measured by GC with a TCD detector, comparing hydrogen production with A) deposition time using a 0.15 mg/mL Pd precursor solution, and B) extended reaction times, highlighting the longevity of the 0.15-Pd-18/TiO_2/MOFC system.

Regardless of other synthetic parameters, systems made with either 0.05 or 0.45 mg/mL of Pd precursor solution were comparatively inactive, producing ≤ 0.04 mL of hydrogen after 8 hours (Figures S16 & S17), despite possessing similar Pd loadings (Table S1) to the active 0.15 mg/mL series. This suggests the Pd nanoparticle size is a key factor. The larger nanoparticles made with a 0.45 mg/mL Pd solution (Figures 6C and S15F), have poor activity, likely due to smaller proportion of surface defects, lower metal surface area per particle, and particle clustering (as observed through TEM). Conversely, the smaller particles made with a 0.05 mg/mL Pd solution have a larger fraction of Pd-C, compared to Pd-Pd, limiting the metallic component of these nanoparticles, making them less effective.

The 0.15 mg/mL Pd concentration produces active nanoparticles for this reaction (Figure 7A), as all three 0.15 mg/mL systems outperform the other MOFC samples tested. This is likely due to the correct combination of nanoparticle size, Pd content and nanoparticle dispersion. The deposition time noticeably influences the systems reactivity, as the 3 and 18 hour samples (0.15-Pd-3/TiO_2/MOFC and 0.15-Pd-18/TiO_2/MOFC) outperform the 1 hour sample (0.15-Pd-1/TiO_2/MOFC). The comparatively poor performance of the 1 hour sample is likely due to the lower Pd content, thus longer deposition times are required to optimise these systems. The 3 hour sample (0.15-Pd-3/TiO_2/MOFC) shows superior hydrogen production over an 8 hour time period (0.21 mL), though plateaus after 6 hours. The 18 hour sample (0.15-Pd-18/TiO_2/MOFC) produces less hydrogen over this 8 hour period (0.17 mL), but does so at a constant rate. These two species were tested over an extended 24 hour period to explore their lifetime (Figure 7B). The 0.15-Pd-3/TiO_2/MOFC species showed no significant hydrogen production after 6 hours, suggesting deactivation. However, 0.15-Pd-18/TiO_2/MOFC keeps reacting at a constant rate, going from 0.17 mL at 8 hours to 0.43 mL after 24 hours. This shows the longer deposition time drastically improves the systems lifetime, and productivity over a longer period. TEM images of the 0.15-Pd-18/TiO_2/MOFC system, both before and after the photocatalytic process (Figures S14C and S14D), show a similar average nanoparticle size (Figures S15D and S15E). This suggests the nanoparticles have not agglomerated during the reaction, explaining the improved lifetime of this system. This shows that this technology, and materials, could be well-suited to initiating long-term continuous photocatalytic reactions.

As such varying the metal precursor concentration and deposition time, can control both the nanoparticle size and Pd loading, within these novel photocatalytic microreactor, demonstrating a clear effect on the activity and lifetime of the system. The control on catalytic activity shows considerable scope for optimising these novel photocatalytic microreactors. Despite the low loading of our MOFC systems (< 0.1 wt%), the efficiency of the system (hydrogen produced per hr per gram of catalyst, 70.4 mL/hr/$g_{catalyst}$) surpassed analogous liquid-phase powdered systems (14 mL/hr/$g_{catalyst}$)[19] by a factor of 5 (calculation in supporting information, page S17). This is likely due to the utilisation of optical fibre technology, serving as an effective, and improved, photon-delivery system, representing an advancement in photonic catalysis.

Conclusion

We have shown, for the first time, microstructured optical fibre canes (MOFCs) can be utilised as hosts for photocatalytic entities, thereby forming a photocatalytic microreactor. Given the necessary choice of host and the small amounts of photocatalyst present, typical characterisation methods are not readily applicable. As such we have used a wide range of characterisation techniques to confirm the integrity and deposition of the photocatalyst; Pd/TiO_2, onto the fused silica cane. In particular, microfocus X-ray absorption spectroscopy, plays a key role in identifying areas of interest, determining structural information by means of X-ray diffraction and X-ray absorption spectroscopy on these regions. The robust nature of our synthetic strategy shows many synthetic variables are readily controlled, and modulated, to tailor the Pd/TiO_2/MOFC photocatalytic systems. This offers significant scope for optimising photocatalytic performance, and lifetime, of coated MOFC systems towards a variety of photocatalytic processes, in this case, hydrogen generation from indirect water splitting.

We believe the use of optical fibre technology has advantages over analogous powder-based methods, with significant potential for the development of new photocatalytic systems, reactors and technology, for a wide range of sustainable applications.

Acknowledgements

MEP, RR, TB and PJAS are grateful to EPSRC for funding (EP/N013883/1, "Adventures in Energy"). AOE and MEP acknowledge Total "Catalysts for the Future" project for funding. RR and DJS also acknowledge the EU Horizon 2020 project "MULTI-site organic-inorganic HYbrid CATalysts for MULTI-step chemical processes (MULTI2HYCAT)" EU 720783 for funding. We acknowledge MEDAC Ltd for help with ICP analysis of these samples. The bio-imaging unit at the University of Southampton are thanked for their help obtaining TEM images. X-ray absorption spectroscopy (XAS) data was collected at B18 at the Diamond Light Source, Didcot, UK via rapid access proposal SP21199. Microfocus X-ray absorption spectroscopy was performed at I18 at the Diamond Light Source, Didcot, UK via standard access proposal SP17819.

Supplementary information

Supplementary information is available including detailed experimental methodologies, fluorescence spectra, UV/Vis spectra, ICP analysis, EXAFS data and analysis, further TEM images with associated nanoparticle distributions and catalytic data. A video from our computed tomography work is also included showing 2D (xy) slices of our TiO_2 coated MOFC, travelling in the z (vertical) direction of the cane.

References

1. Sanz-Pérez, E. S.; Murdock, C. R.; Didas, S. A.; Jones, C. W. Direct Capture of CO_2 from Ambient Air. *Chem. Rev.* **2016**, *116*, 11840-11876.
2. McGlade, C.; Ekins, P. The geographical distribution of fossil fuels unused when limiting global warming to 2 °C. *Nature* **2015**, *517*, 187-190.
3. Chu, S.; Cui, Y.; Liu, N. The path towards sustainable energy. *Nature Mater.* **2017**, *16*, 16-22.
4. Friend, C. M.; Xu, B. Heterogeneous Catalysis: A Central Science for a Sustainable Future. *Acc. Chem. Res.* **2017**, *50*, 517-521.
5. Corrigan, N.; Shanmugam, S.; Xu, J.; Boyer, C. Photocatalysis in organic and polymer synthesis. *Chem. Soc. Rev.* **2016**, *45*, 6165-6162.
6. Chen, J. R.; Hu, X. Q.; Lu, L. Q.; Xiao, W. J. Exploration of Visible-Light Photocatalysis in Heterocycle Synthesis and Functionalization: Reaction Design and Beyond. *Acc. Chem. Res.* **2016**, *49*, 1911-1923.
7. Osterloh, F. E. Inorganic Materials as Catalysts for Photochemical Splitting of Water. *Chem. Mater.* **2008**, *20*, 35-54.
8. Maeda, K.; Domen, K. Photocatalytic Water Splitting: Recent Progress and Future Challenges. *J. Phys. Chem. Lett.* **2010**, *1*, 2655-2661.
9. Ahmad, H.; Kamarudin, S. K.; Minggu, L. J.; Kassim, M. Hydrogen from photo-catalytic water splitting process: A review. *Renew. Sust. Energ. Rev.* **2015**, *43* 599-610.
10. Christoforidis, K. C.; Fornasiero, P. Photocatalytic Hydrogen Production: A Rift into the Future Energy Supply. *ChemCatChem* **2017**, *9*, 1523-1544.
11. Stolarczyk, J. K.; Bhattacharyya, S.; Polavarapu, L.; Feldmann, J. Challenges and Prospects in Solar Water Splitting and CO_2 Reduction with Inorganic and Hybrid Nanostructures. *ACS Catal.* **2018**, *8*, 3602-3635.
12. Kleij, A. W.; North, M.; Urakawa, A. CO_2 Catalysis. *ChemSusChem* **2017**, *10*, 1036-1038.
13. Zhang, G.; Sun, S.; Jiang, W.; Miao, X.; Zhao, Z.; Zhang, X.; Qu, D.; Zhang, D.; Li, D.; Sun, Z. A Novel Perovskite $SrTiO_3$-Ba_2FeNbO_6 Solid Solution for Visible Light Photocatalytic Hydrogen Production. *Adv. Energy Mater.* **2017**, *7*, 1600932.
14. Yue, Q.; Wan, Y.; Sun, Z.; Wu, X.; Yuan, Y.; Du, P. MoP is a novel, noble-metal-free cocatalyst for enhanced photocatalytic hydrogen production from water under visible light. *J. Mater. Chem. A* **2015**, *3*, 16941-16947.

15. Leithall, R. M.; Shetti, V. N.; Maurelli, S.; Chiesa, M.; Gianotti, E.; Raja, R. Toward understanding the catalytic synergy in the design of bimetallic molecular sieves for selective aerobic oxidations. *J. Am. Chem. Soc.* **2013**, *135*, 2915-2918.
16. Moniz, S. J. A.; Shevlin, S. A.; Martin, D. J.; Guo, Z. X.; Tang, J. Visible-light driven heterojunction photocatalysts for water splitting – a critical review. *Energy Environ. Sci.* **2015**, *8*, 731-759.
17. Serra, M.; Albero, J.; Garcia, H. Photocatalytic Activity of Au/TiO_2 Photocatalysts for H_2 Evolution: Role of the Au Nanoparticles as a Function of the Irradiation Wavelength. *ChemPhysChem* **2015**, *16*, 1842-1845.
18. Bowker, M.; Morton, C.; Kennedy, J.; Bahruji, H.; Greves, J.; Jones, W.; Davies, P. R.; Brookes, C.; Wells, P. P.; Dimitratos, N. Hydrogen production by photoreforming of biofuels using Au, Pd and Au–Pd/TiO_2 photocatalysts. *J. Catal.* **2014**, *310*, 10-15.
19. Bahruji, H.; Bowker, M.; Davies, P. R.; Morgan, D. J.; Morton, C. A.; Egerton, T. A.; Kennedy, J.; Jones, W. Rutile TiO_2–Pd Photocatalysts for Hydrogen Gas Production from Methanol Reforming. *Top. Catal.* **2015**, *58*, 70-76.
20. Winzer, P. J.; Neilson, D. T.; Chraplyvy, A. R. Fiber-optic transmission and networking: the previous 20 and the next 20 years. *Optics Express* **2018**, *26*, 24190-24239.
21. Cheng, Q.; Bahadori, M.; Glick, M.; Rumley, S.; Bergman, K. Recent advances in optical technologies for data centers: a review. *Optica* **2018**, *5*, 1354-1370.
22. Amezcua-Correa, A.; Yang, J.; Finlayson, C. E.; Peacock, A. C.; Hayes, J. R.; Sazio, P. J. A.; Baumberg, J. J.; Howdle, S. M. Surface enhanced Raman scattering using microstructured optical fibre substrates. *Adv. Funct. Mater.* **2007**, *17*, 2024-2030.
23. Zhang, N.; Liu, H.; Stolyarov, A. M.; Zhang, T.; Li, K.; Shum, P. P.; Fink, Y.; Sun, X. W.; Wei, L. Azimuthally polarized radial emission from a quantum dot fiber laser. *ACS Photonics* **2016**, *3*, 2275-2279.
24. Denny, F.; Scott, J.; Pareek, V.; Peng, G. D.; Amal, R. CFD modelling for a TiO_2-coated glass-bead photoreactor irradiated by optical fibres: Photocatalytic degradation of oxalic acid. *Chem. Eng. Sci.* **2009**, *64*, 1695-1706.
25. Ola, O.; Maroto-Valer, M. M. Role of catalyst carriers in CO_2 photoreduction over nanocrystalline nickel loaded TiO2-based photocatalysts. *J. Catal.* **2014**, *309*, 300-308.
26. Sazio, P. J. A.; Amezcua-Correa, A.; Finlayson, C. E.; Hayes, J. R.; Scheidemantel, T. J.; Baril, N. F.; Jackson, B. R.; Won, D. J.; Zhang, F.; Margine, E. R.; Gopalan, V.; Crespi, V. H.; Badding, J. V. Microstructured Optical Fibers as High-Pressure Microfluidic Reactors. *Science* **2006**, *311*, 1583-1586.
27. Egusa, S.; Wang, Z.; Chocat, N.; Ruff, Z. M.; Stolyarov, A. M.; Shemuly, D.; Sorin, F.; Rakich, P. T.; Joannopoulos, J. D.; Fink, Y. Multimaterial piezoelectric fibres. *Nature Mater.* **2010**, *9*, 643-648.
28. Baril, N. F.; He, R.; Day, T. D.; Sparks, J. R.; Keshavarzi, B.; Krishnamurthi, M.; Borhan, A.; Gopalan, V.; Peacock, A. C.; Healy, N.; Sazio, P. J. A.; Badding, J. V. Confined high-pressure chemical deposition of hydrogenated amorphous silicon. *J. Am. Chem. Soc.* **2012**, *134*, 19-22.
29. Edwards, J. K.; Ntainjua N., E.; Carley, A. F.; Herzing, A. A.; Kiely, C. J.; Hutchings, G. J. Direct Synthesis of H_2O_2 from H_2 and O_2 over Gold, Palladium, and Gold–Palladium Catalysts Supported on Acid-Pretreated TiO_2. *Angew. Chem. Int. Ed.* **2009**, *48*, 8512-8515.
30. Couny, F.; Benabid, F.; Light, P. S. Large pitch kagome-structured hollow-core photonic crystal fiber. *Optics Lett.* **2006**, *31*, 3574-3576.
31. Shiraishi, Y.; Hirakawa, H.; Togawa, Y.; Sugano, Y.; Ichikawa, S.; Hirai, T. Rutile Crystallites Isolated from Degussa (Evonik) P25 TiO_2: Highly Efficient Photocatalyst for Chemoselective Hydrogenation of Nitroaromatics. *ACS Catal.* **2013**, *3*, 2318-2326.
32. Chen, X.; Mao, S. S. Titanium Dioxide Nanomaterials: Synthesis, Properties, Modifications, and Applications. *Chem. Rev.* **2007**, *107*, 2891-2959.
33. Quesada-Cabrera, R.; Mills, A.; O'Rourke, C. Action spectra of P25 TiO_2 and a visible light absorbing, carbon-modified titania in the photocatalytic degradation of stearic acid. *Appl. Catal. B: Environ.* **2014**, *150-151*, 338-344.
34. Paredis, K.; Ono, L. K.; Behafarid, F.; Zhang, Z.; Yang, J. C.; Frenkel, A. I.; Cuenya, B. R. Evolution of the Structure and Chemical State of Pd Nanoparticles during the in Situ Catalytic Reduction of NO with H_2. *J. Am. Chem. Soc.* **2011**, *133*, 13455-13464.
35. Clayton, K. N.; Salameh, J. W.; Wereley, S. W.; Kinzer-Ursem, T. L. Physical characterization of nanoparticle size and surface modification using particle scattering diffusometry. *Biomicrofluidics* **2016**, *10*, 0547107.
36. Choi, H. J.; Kang, M. Hydrogen production from methanol/water decomposition in a liquid photosystem using the anatase structure of Cu loaded TiO_2. *Int. J. Hydro. Energy* **2007**, *32*, 3841-3848.
37. Hainer, A. S.; Hodgins, J. S.; Sandre, V.; Vallieres, M.; Lanterna, A. E.; Scaiano, J. C. Photocatalytic Hydrogen Generation Using Metal-Decorated TiO_2: Sacrificial Donors vs True Water Splitting. *ACS Energy Lett.* **2018**, *3*, 542-545.
38. Fang, S.; Sun, Z.; Hu, Y. H. Insights into the Thermo-Photo Catalytic Production of Hydrogen from Water on a Low-Cost NiO_x-Loaded TiO_2 Catalyst. *ACS Catal.* **2019**, *9*, 5047-5056.